ACSNANO

www.acsnano.org

ARTICLE

# Metal Hydrides with In Situ Built Electron/Ion Dual-Conductive Framework for Stable All-Solid-State Li-Ion Batteries

Panyu Gao, Shunlong Ju, Zipeng Liu, Guanglin Xia,* Dalin Sun, and Xuebin Yu*

Cite This: *ACS Nano* 2022, 16, 8040−8050

Read Online

ACCESS | Metrics & More | Article Recommendations | Supporting Information

**ABSTRACT:** Due to their high theoretical specific capacity, metal hydrides are considered to be one of the most promising anode material for all-solid-state Li-ion batteries. Their practical application suffers, however, from the poor cycling stability and sluggish kinetics. Herein, we report the in situ fabrication of $MgH_2$ and $Mg_2NiH_4$ that are uniformly space-confined by inactive $Nd_2H_5$ frameworks with high Li-ion and electron conductivity through facile hydrogenation of single-phase $Nd_4Mg_{80}Ni_8$ alloys. The formation of $MgH_2$ and $Mg_2NiH_4$ nanocrystals could not only shorten Li-ion and electron diffusion pathways of the whole electrode but also relieve the induced stress upon volume changes. Additionally, the robust frameworks constructed by homogeneous distribution of inactive $Nd_2H_5$ based on a molecular level could effectively alleviate the volume expansion and phase separation of thus-confined $MgH_2$ and $Mg_2NiH_4$. More importantly, it is theoretically and experimentally verified that the uniform distribution of $Nd_2H_5$, which is an electronic conductor with a Li-ion diffusion barrier that is much lower than that of $MgH_2$ and $Mg_2NiH_4$, could further facilitate the electron and Li-ion transfer of $MgH_2$ and $Mg_2NiH_4$. Consequently, the space-confined $MgH_2$ and $Mg_2NiH_4$ deliver a reversible capacity of 997 mAh $g^{-1}$ at 2038 mA $g^{-1}$ after 100 cycles.

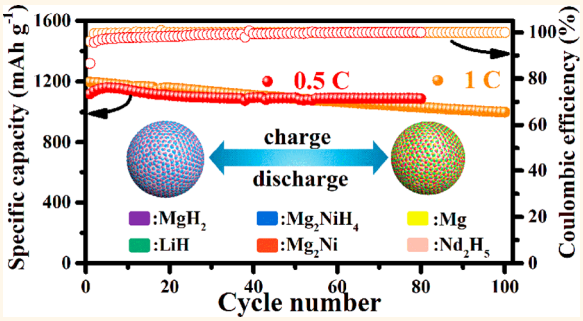


**KEYWORDS:** *all-solid-state Li-ion batteries, metal hydrides, magnesium hydride, Li storage performance, cycling stability*

The rapid development of electronic vehicles and energy storage devices has stimulated the ever-growing requirements of Li-ion batteries (LIBs) with high energy density by exploring various emerging high-capacity anodes.[1−4] Among the recently developed anodes, metal hydrides have been widely regarded as one of the promising candidates due to their ultrahigh theoretical Li storage capacity (e.g., 2032 mAh $g^{-1}$ for $MgH_2$) based on the conversion reaction: $MH_x + xLi^+ + xe^- \leftrightarrow M + xLiH$.[5−7] Moreover, in comparison to all other conversion electrodes, the lowest value of polarization ever reported could be observed for $MgH_2$, resulting from the facile transportation of hydrogen, which effectively reduces the risk of thermal runaway upon cycling.[8−10] Nevertheless, the poor electronic conductivity of $MgH_2$ particles and the particle agglomeration and phase separation induced by serious volume change[8,11−13] lead to the rapid capacity decay during the charge/discharge cycles using traditional liquid organic electrolytes. Although these issues could be improved by building nanostructured anodes of $MgH_2$ to a large extent, the continuous and rapid decay of reversible capacity of $MgH_2$ is still observed due to the inevitable detrimental reactions between electrodes and electrolytes.[14] In addition, the liquid organic electrolytes intrinsically hold the drawbacks of flammability, leakage, and electrochemical instability, which triggers severe safety issues, especially in large-scale energy storage systems.[15−19]

To effectively solve the safety issues of LIBs, all-solid-state LIBs (ASSLIBs) using lithium borohydrides as the electrolytes have been developed toward practical application of metal hydrides.[20−23] $LiBH_4$ could not only act as the solid-state electrolyte due to its high Li-ion conductivity, which is comparable to that of liquid organic electrolytes, but also promote $H^-$ conductivity owing to the hydrogen exchange effect between $LiBH_4$ and $MgH_2$, which is capable of facilitating the reversibility of metal hydrides for reversible Li storage.[24−26] Unfortunately, due to the insulating nature of

Received: January 29, 2022
Accepted: May 9, 2022
Published: May 11, 2022

Downloaded via FUDAN UNIV on August 7, 2022 at 05:19:36 (UTC).
See https://pubs.acs.org/sharingguidelines for options on how to legitimately share published articles.

ACS Publications © 2022 American Chemical Society



https://doi.org/10.1021/acsnano.2c01038
*ACS Nano* 2022, 16, 8040−8050

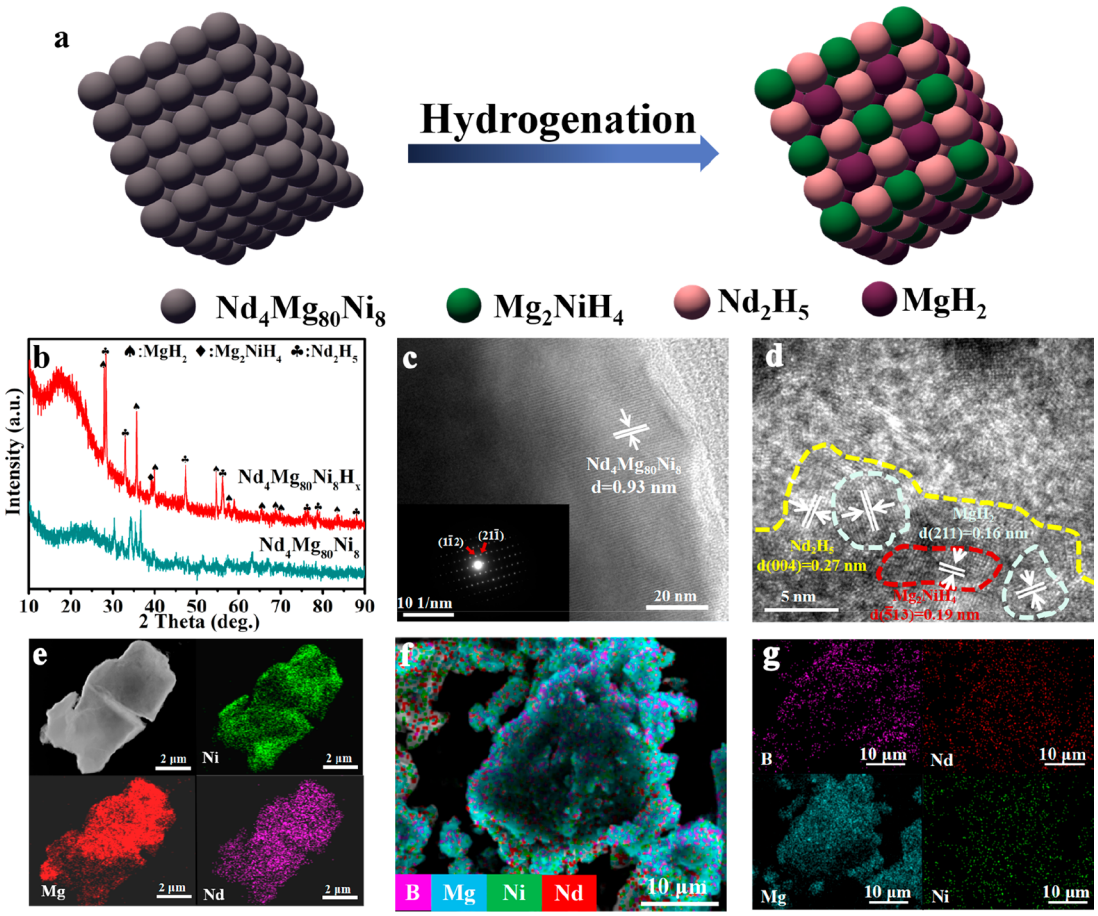


**Figure 1. (a) Schematic illustration for the fabrication of space-confined $MgH_2$ and $Mg_2NiH_4$ into inactive $Nd_2H_5$ frameworks. (b) XRD patterns of the as-synthesized single-phase $Nd_4Mg_{80}Ni_8$ alloy and $Nd_4Mg_{80}Ni_8H_x$. (c) TEM image of single-phase $Nd_4Mg_{80}Ni_8$ alloy. The inset shows the corresponding selected area electron diffraction pattern of one single particle. (d) HRTEM image of the as-synthesized $Nd_4Mg_{80}Ni_8H_x$. (e) TEM image of the as-synthesized $Nd_4Mg_{80}Ni_8H_x$ and the corresponding EDS elemental mapping images of Ni, Mg, and Nd. (f,g) EDS elemental mapping images of ball-milled composite of the as-synthesized $Nd_4Mg_{80}Ni_8H_x$, $LiBH_4$, and Super P as the electrode.**

$MgH_2$ and the large volume change induced by the conversion reaction, rapid capacity decay could still be observed during the cycling charge and discharge process.[27] Although the Li storage performance of $MgH_2$ could be enhanced to a large extent with the assistance of catalysts,[25,28,29] the intrinsic Li ion and electronic transport between the electrode and the electrolyte of ASSLIBs when using $LiBH_4$ as the solid-state electrolyte is greatly limited. As a result, it is necessary to develop an efficient and stable electron/ion dual-conductive pathway to boost the Li storage performance of metal hydrides.

Bearing these considerations in mind, herein, we report an efficient way to fabricate metal-hydride-based anodes with in situ built electron/ion dual-conductive frameworks. It is realized by the facile hydrogenation of single-phase $Nd_4Mg_{80}Ni_8$ alloys, leading to the in situ formation of $MgH_2$ and $Mg_2NiH_4$ that are uniformly space-confined by inactive $Nd_2H_5$ frameworks with high Li-ion and electron conductivity (Figure 1a). First, the as-synthesized nanocrystals of $MgH_2$ and $Mg_2NiH_4$ could offer short diffusion paths for electrons and Li ions, which promotes the Li storage reaction rate of metal hydrides. In addition, the homogeneous distribution of inactive $Nd_2H_5$ based on a molecular level could act as a robust and stable framework, which could effectively alleviate the large volume expansion of thus-confined $MgH_2$ and $Mg_2NiH_4$ and prevent the phase separation upon cycling, leading to good preservation of the structural integrity of the whole electrode. More importantly, both theoretical calculation and experimental observation demonstrate that $Nd_2H_5$ is an electronic conductor with a Li-ion diffusion barrier that is much lower than that of $MgH_2$ and $Mg_2NiH_4$, and hence its uniform distribution could further facilitate electron and Li-ion transfer of $MgH_2$ and $Mg_2NiH_4$. In addition, both $Nd_2H_5$ and $Mg_2NiH_4$ play a catalytic role in effectively weakening Mg−H bonds of $MgH_2$, which could kinetically promote reversible charge and discharge performance of $MgH_2$. As a result, the hydrogenated $Nd_4Mg_{80}Ni_8$ electrode exhibits an impressive reversible capacity of 997 mAh $g^{-1}$ after 100 cycles at a high current density of 2038 mAh $g^{-1}$ with a high initial Coulombic efficiency of 92.2%.

## RESULTS AND DISCUSSION

After a facile thermal annealing process, the X-ray diffraction (XRD) pattern (Figure 1b) demonstrates the uniform formation of the single-phase $Nd_4Mg_{80}Ni_8$ alloy, corresponding well with the selected area electron diffraction (SAED) pattern (Figure 1c). Scanning electron microscopy (SEM) measurement illustrates an average particle size of approximately 6.4 $\mu$m for the as-prepared $Nd_4Mg_{80}Ni_8$ alloy (Figure S1a). Subsequently, the repeated hydrogenation and hydrogenation process of the thermally annealed alloys leads to in situ


https://doi.org/10.1021/acsnano.2c01038
ACS Nano 2022, 16, 8040−8050

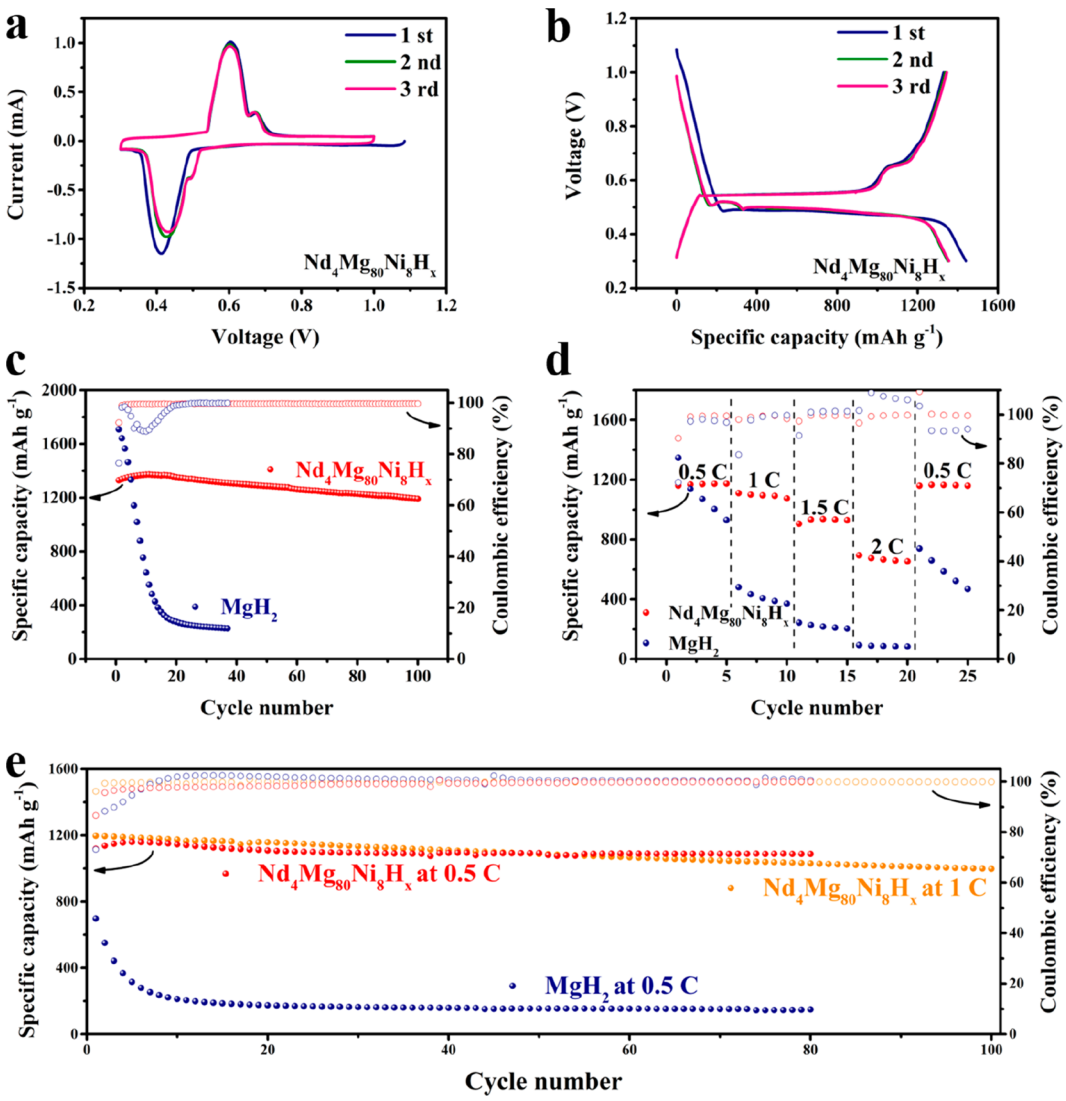


**Figure 2. (a) CV profiles of the $Nd_4Mg_{80}Ni_8H_x$ electrode for the initial three cycles at a scan rate of 0.025 mV $s^{-1}$. (b) Galvanostatic discharge−charge curves of the $Nd_4Mg_{80}Ni_8H_x$ electrode at 0.1C for the initial three cycles. (c) Cycling performance and (d) rate capability of the $Nd_4Mg_{80}Ni_8H_x$ electrode at 0.1C. (e) Cycling performance of the $Nd_4Mg_{80}Ni_8H_x$ electrode at 0.5 and 1C.**

formation of $MgH_2$, $Nd_2H_5$, and $Mg_2NiH_4$ phases (denoted as $Nd_4Mg_{80}Ni_8H_x$), as verified by XRD results (Figure 1b). A high-resolution transmission electron microscopy (HRTEM) image of the hydrogenated $Nd_4Mg_{80}Ni_8$ (Figure 1d) illustrates that the thus-obtained hydrides exhibit distinct lattice fringe of 0.16, 0.27, and 0.19 nm, corresponding to the (211) plane of $MgH_2$, the (004) plane of $Nd_2H_5$, and the ($\bar{5}13$) plane of $Mg_2NiH_4$, respectively, which provides additional evidence for the formation of $MgH_2$, $Mg_2NiH_4$, and $Nd_2H_5$. In addition, $Nd_4Mg_{80}Ni_8H_x$ delivers a $H_2$ desorption capacity of 5.64 wt %, indicating the complete hydrogenation of the $Nd_4Mg_{80}Ni_8$ alloy (Figure S2). Interestingly, owing to the uniform distribution of Nd, Mg, and Ni inside the single-phase $Nd_4Mg_{80}Ni_8$ alloys at the atom level, the homogeneous distribution of the thus-formed nanocrystals of hydrides could be clearly observed with a size ranging from 5 to 10 nm, which could be further supported by the corresponding energy-dispersive spectroscopy (EDS) elemental mapping results (Figure 1e). As verified by SEM results, the average particle size of the as-synthesized $Nd_4Mg_{80}Ni_8H_x$ is slightly larger than that of $MgH_2$ used in this work (Figure S1b,c). The $Nd_4Mg_{80}Ni_8H_x$ anode is subsequently fabricated by mixing $LiBH_4$ as the solid-state electrolyte and Super P as the electronic conductor with the size of the particles ranging from 5 to 25 $\mu$m (Figure S1d), which are slightly decreased compared with the original hydrogenated $Nd_4Mg_{80}Ni_8$ particles (Figure S1b). Moreover, the elemental mapping results over the hydrogenated $Nd_4Mg_{80}Ni_8$ particles (Figure 1f,g) illustrate that the Nd, Mg, Ni, and B elements are uniformly distributed in the particles, validating a homogeneous distribution of the electroactive material, electrolyte, and conductive carbon after a simple mechanical milling process.

Cyclic voltammetry (CV) measurements reveal a strong reduction peak at 0.42 V during the first discharge process of the as-synthesized $Nd_4Mg_{80}Ni_8H_x$ (Figure 2a), which could be attributed to the reduction of $MgH_2$ and $Mg_2NiH_4$ with the formation of Mg and $Mg_2Ni$ as the discharged products accompanied by the complete disappearance of $MgH_2$ and $Mg_2NiH_4$, as verified by the XRD results (Figure 3a). It is interesting to note that $Nd_2H_5$ that is uniformly distributed inside $Nd_4Mg_{80}Ni_8H_x$ could still be observed after full lithiation upon discharging to 0.3 V (Figure 3a), which


https://doi.org/10.1021/acsnano.2c01038
ACS Nano 2022, 16, 8040−8050

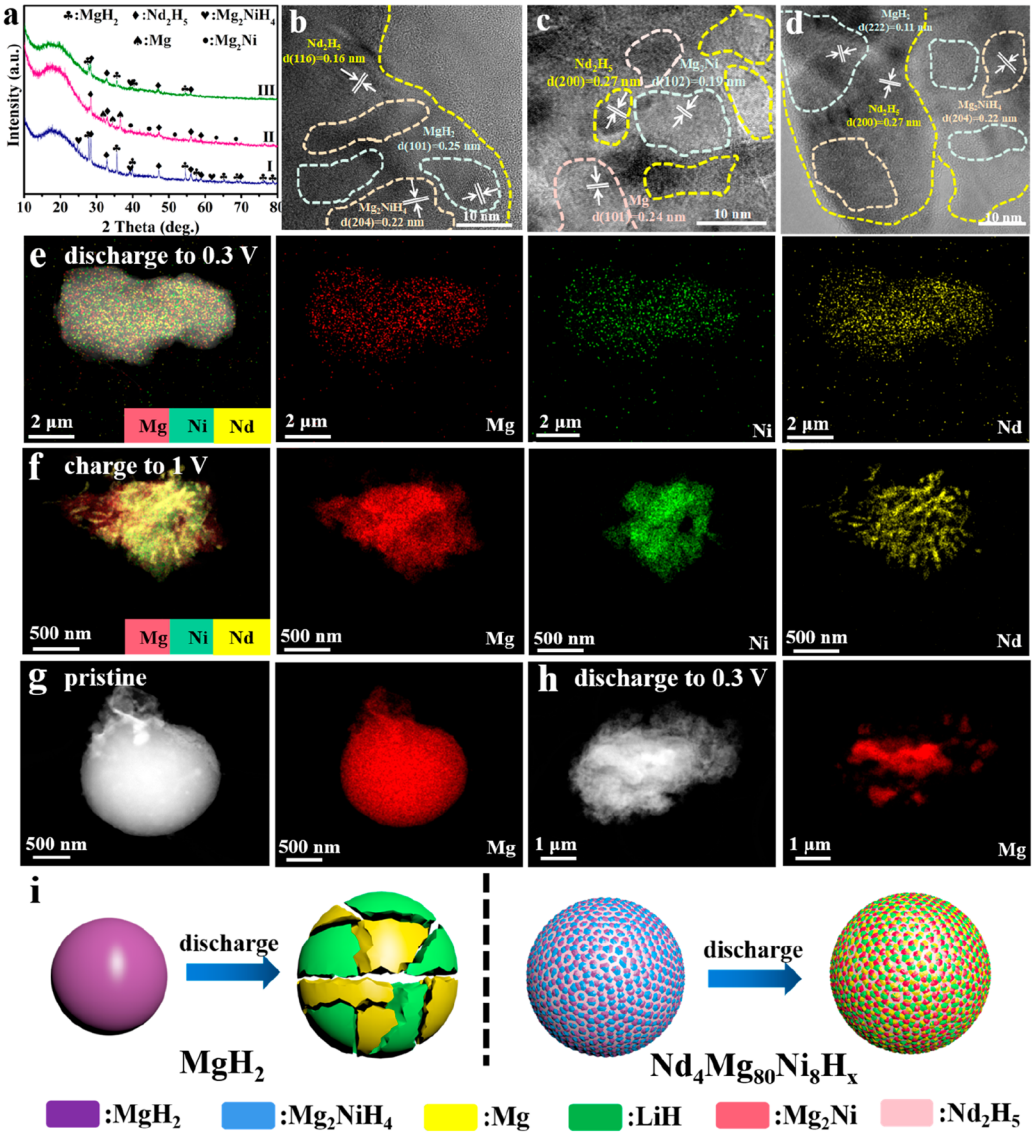


**Figure 3. (a) XRD patterns of the $Nd_4Mg_{80}Ni_8H_x$ electrode at various discharge and charge states: (I) fresh electrode, (II) after initial discharge process to 0.3 V, and (III) after the initial charge process to 1.0 V. HRTEM images of the $Nd_4Mg_{80}Ni_8H_x$ electrode at various states: (b) before cycling, (c) after the initial discharge to 0.3 V, and (c) after the initial charge to 1.0 V. Elemental mapping results of the $Nd_4Mg_{80}Ni_8H_x$ electrode at various states: (e) after the complete discharge to 0.3 V and (f) after complete charge to 1.0 V. Scanning TEM (STEM) images and the corresponding elemental mapping results of the $MgH_2$ electrode at various states: (g) pristine and (h) after complete discharge to 0.3 V. (i) Schematic illustration of the charge and discharge process of $MgH_2$ and $Nd_4Mg_{80}Ni_8H_x$ electrodes.**

could serve as a structural support to alleviate the volume change of $MgH_2$ and $Mg_2NiH_4$ upon cycling. The corresponding HRTEM image (Figure 3c) illustrates distinct lattices fringed with 0.19, 0.24, and 0.27 nm, corresponding to the (102) planes of $Mg_2Ni$, the (101) planes of Mg, and the (200) planes of $Nd_2H_5$, respectively, in good agreement with the XRD results. Conversely, two anodic peaks located at 0.57 and 0.65 V in the first charge cycle could be ascribed to the regeneration of $MgH_2$ and $Mg_2NiH_4$, respectively, corresponding well with the XRD results (Figure 3a). As shown in Figure 3a, the characteristic diffraction peaks of $MgH_2$ and $Mg_2NiH_4$ emerge again with the presence of $Nd_2H_5$ upon charging to 1 V. After the complete delithiation process, the marked *d*-spacings of the crystalline nanocrystals are measured to be 0.11, 0.27, and 0.22 nm, corresponding to the (222) plane of $MgH_2$, the (200) plane of $Nd_2H_5$, and the (204) plane of $Mg_2NiH_4$, respectively (Figure 3d). As a result, the reversible Li storage of the $Nd_4Mg_{80}Ni_8H_x$ electrode could be concluded as the reversible conversion reactions of $MgH_2$ and $Mg_2NiH_4$ as shown below.

$$MgH_2 + 2Li^+ + 2e^- \leftrightarrow Mg + 2LiH \quad (1)$$

$$Mg_2NiH_4 + 4Li^+ + 2e^- \leftrightarrow Mg_2Ni + 4LiH \quad (2)$$

Except for the initial cycle, the CV curves in the subsequent cycles almost overlap without observation of an irreversible reaction, suggesting its good reversibility and high Coulombic efficiency. The electrochemical performance of $Nd_4Mg_{80}Ni_8H_x$ is further investigated using galvanostatic discharge−charge curves (Figure 2b). The small potential differences between the charge and discharge plateau provide additional evidence for the good electrochemical reversibility of $Nd_4Mg_{80}Ni_8H_x$ for


https://doi.org/10.1021/acsnano.2c01038
ACS Nano 2022, 16, 8040−8050

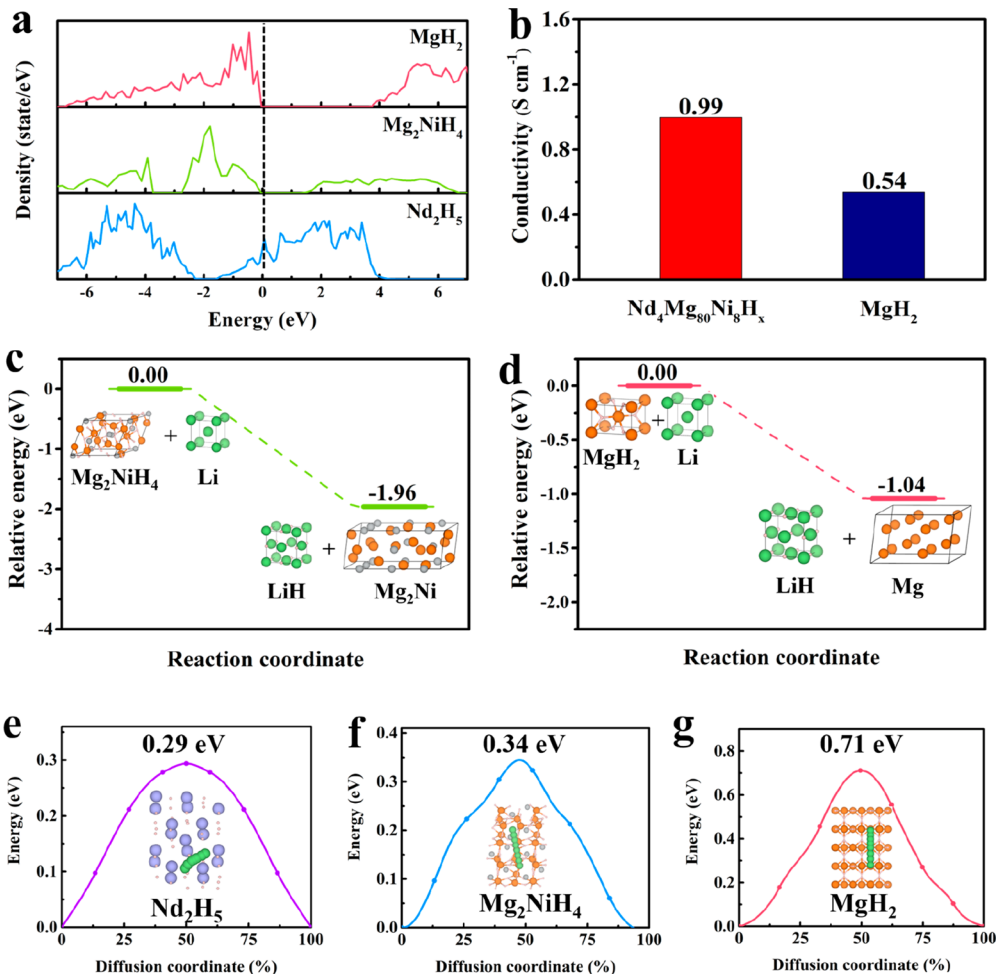


**Figure 4. (a) Density of states of $MgH_2$, $Mg_2NiH_4$, and $Nd_2H_5$. (b) Charge conductivity of the $Nd_4Mg_{80}Ni_8H_x$ and $MgH_2$ electrodes tested by chronoamperometry. Energy curves of lithiation process of $MgH_2$ (c) and $Mg_2NiH_4$ (d). The inset shows the corresponding schematic illustration. The energy barrier of Li diffusion on the surface of (e) $Nd_2H_5$, (f) $Mg_2NiH_4$, and (g) $MgH_2$. Green, silver, pink, orange, and purple spheres are Li, Ni, H, Mg, and Nd, respectively.**

Li storage. The initial discharge capacity of the $Nd_4Mg_{80}Ni_8H_x$ electrode reaches 1440 mAh $g^{-1}$, slightly higher than its theoretical value of the theoretical capacity (i.e., 1352 mAh $g^{-1}$ calculated based on the following equation, $C_{(Nd_4Mg_{80}Ni_8H_x)} = C_{(MgH_2)} \times$ %mass of $MgH_2$ + $C_{(Mg_2NiH_4)} \times$ %mass of $Mg_2NiH_4$, which could be possibly induced by the slight alloying reaction of extra Mg with Li. More importantly, a reversible charge capacity of 1392 mAh $g^{-1}$ could be obtained in the first cycle, corresponding to an initial Coulombic efficiency (ICE) of 92.2%, providing direct evidence for the high reversibility of the $Nd_4Mg_{80}Ni_8H_x$ electrode. Although both discharge and charge capacities of the $Nd_4Mg_{80}Ni_8H_x$ electrode of the first cycle are much lower than those of the $MgH_2$ electrode due to the introduction of Nd and Ni with large weight, the initial Coulombic efficiency for the $MgH_2$ electrode is only 76.4%. More importantly, upon repeated processing for Li storage performance, the $Nd_4Mg_{80}Ni_8H_x$ electrode delivers a high reversible capacity of 1191 mAh $g^{-1}$ after 100 cycles, corresponding to a capacity retention of 89.6%. By comparison, the capacity of the $MgH_2$ electrode rapidly decays to less than 300 mAh $g^{-1}$ after only 18 cycles.

The rate capability of the $Nd_4Mg_{80}Ni_8H_x$ electrode, a key indicator for practical application of ASSLIBs, is subsequently investigated. As shown in Figure 2d, the $Nd_4Mg_{80}Ni_8H_x$ electrode exhibits an excellent rate performance, delivering an average reversible capacity of 1110 mAh $g^{-1}$ at 1C. Upon increasing the current density to 2C, a reversible specific capacity as high as 694 mAh $g^{-1}$ could still be achieved. By comparison, the reversible specific capacity of $MgH_2$ rapidly decreases to only 93 mAh $g^{-1}$ at 2C. More importantly, the reversible capacity returns to 1160 mAh $g^{-1}$ with nearly no capacity fading when the current density returns to 0.5C, which demonstrates the capability of the $Nd_4Mg_{80}Ni_8H_x$ electrode toward fast Li-ion storage and extraction. Subsequently, the cycling performance of the $Nd_4Mg_{80}Ni_8H_x$ electrode is investigated at the high current density of 0.5 and 1C. After 80 cycles, a high reversible capacity of 1087 mAh $g^{-1}$ could still be obtained (Figure 2e), corresponding to an ultrahigh capacity retention of 97.2%. It should be noted that the reversible capacity of the $Nd_4Mg_{80}Ni_8H_x$ electrode is gradually increased in the initial six cycles, which could be possibly attributed to the activation of $MgH_2$ and $Mg_2NiH_4$ during the cycling. By comparison, the reversible capacity of the $MgH_2$ electrode fades rapidly to 200 mAh $g^{-1}$ after only 10 cycles at a low current density of 0.5C. Impressively, upon increasing the current density to 1C, the initial reversible capacity of the $Nd_4Mg_{80}Ni_8H_x$ electrode still reaches 1196 mAh $g^{-1}$ with a high Coulombic efficiency of 96%, and this


https://doi.org/10.1021/acsnano.2c01038
ACS Nano 2022, 16, 8040−8050

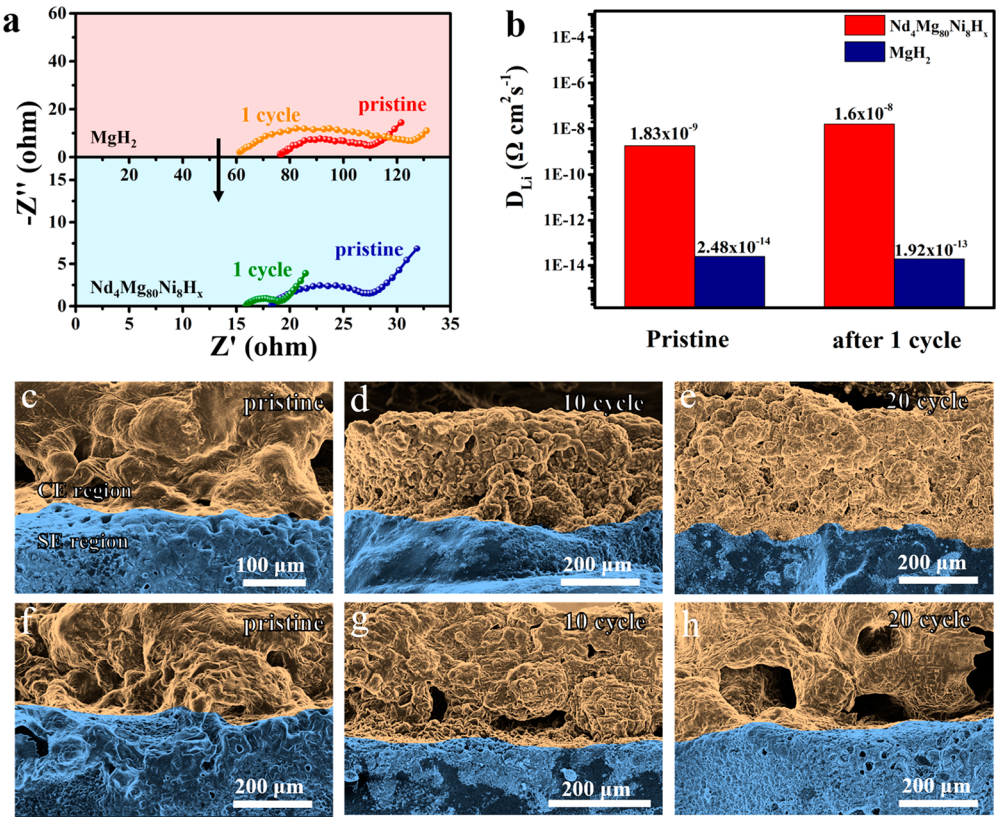


**Figure 5. (a) EIS profiles of the $Nd_4Mg_{80}Ni_8H_x$ after different cycles at 0.1C. (b) Diffusion coefficient of Li ions of the $Nd_4Mg_{80}Ni_8H_x$ and $MgH_2$ electrodes at different cycles at 0.1C. Cross-sectional SEM images of the $Nd_4Mg_{80}Ni_8H_x$ (c−e) and $MgH_2$ (f−h) electrodes before and after cycling at 1C.**

value is well-preserved to be 997 mAh $g^{-1}$ after 100 cycles, which is among the best reported metal hydride anodes so far (Figure S3). More importantly, the Coulombic efficiencies of almost 100% are well-maintained during the whole charge and discharge process, which provides additional evidence for the excellent reversibility of the $Nd_4Mg_{80}Ni_8H_x$ electrode. In strong contrast, the pristine $MgH_2$ electrode is damaged after only a few cycles and cannot maintain the charge−discharge cycle at such a high current rate.

As the hydrogenated $Nd_4Mg_{80}Ni_8$ alloys are mainly composed of $Mg_2NiH_4$ and $Nd_2H_5$ in addition to $MgH_2$, their respective role in affecting the electrochemical performance of $MgH_2$ is investigated in detail (Figure S5). The as-synthesized $Mg_2NiH_4$ and $Nd_2H_5$ are irregular in shape with comparable particle sizes ranging from 5 to 10 $\mu$m (Figure S6a,b), and after ball milling with $LiBH_4$ and Super P, the as-formed particles are pulverized to some extent but with comparable particle sizes (Figure S6c,d). The corresponding HRTEM images (Figure S6e,f) exhibit distinct lattice fringes of both $Mg_2NiH_4$ and $MgH_2$ inside the $MgH_2$ electrode after the introduction of $Mg_2NiH_4$ and both $Nd_2H_4$ and $MgH_2$ inside the $MgH_2$ electrode after the introduction of $Nd_2H_5$, indicating the relatively uniform distribution of $Mg_2NiH_4$ and $Nd_2H_5$ in the corresponding electrodes after ball milling. Particularly, the initial reversible capacity of $MgH_2$ could be effectively increased to 1284 mAh $g^{-1}$ with the addition of $Mg_2NiH_4$ and 1418 mAh $g^{-1}$ with the addition of $Nd_2H_5$, respectively. More importantly, the $MgH_2$ electrode delivers a reversible capacity of 871 mAh $g^{-1}$ after 100 cycles due to the introduction of $Mg_2NiH_4$ and 1027 mAh $g^{-1}$ after 86 cycles due to the introduction of $Nd_2H_5$. In strong contrast, only a negligible reversible capacity of 216 mAh $g^{-1}$ could be obtained for pure $MgH_2$ electrodes after 50 cycles. This result directly demonstrates the positive role of $Mg_2NiH_4$ and $Nd_2H_5$ in improving the electrochemical performance of $MgH_2$.

In order to unravel the role of $Mg_2NiH_4$ and $Nd_2H_5$ in improving the electrochemical performance of $MgH_2$, the density of states (DOS) of $MgH_2$, $Mg_2NiH_4$, and $Nd_2H_5$ were first calculated (Figure 4a). It is interesting to note that, although both the $MgH_2$ and $Mg_2NiH_4$ are semiconductors, the band gap of $Mg_2NiH_4$ is much narrower than that of $MgH_2$, which demonstrates the superior diffusion of electrons in $Mg_2NiH_4$ in comparison with $MgH_2$. More importantly, the DOS of $Nd_2H_5$ crosses the Fermi level, indicating that $Nd_2H_5$ is a conductor, which could effectively promote the electronic conductivity of the thus-fabricated $Nd_4Mg_{80}Ni_8H_x$ electrode. This result could be further supported by measuring the direct current (DC) conductivity of the $Nd_4Mg_{80}Ni_8H_x$ electrode (Figure 4b). It is calculated that the DC conductivity of the $Nd_4Mg_{80}Ni_8H_x$ electrode approaches 0.99 S $cm^{-1}$ at 130 °C, which is nearly 2 times higher than that of the pure $MgH_2$ electrode (0.54 S $cm^{-1}$). This result provides direct evidence that the homogeneous distribution of $Mg_2NiH_4$ and $Nd_2H_5$ that is achieved through in situ hydrogenation of single-phase $Nd_4Mg_{80}Ni_8$ alloys is capable of effectively enhancing the electron transfer of the $MgH_2$ electrode, which contributes to enhancing the Li storage performance of $MgH_2$. Additionally, considering the electrochemical activity of $Mg_2NiH_4$ in participating in Li storage performance, the lithiation process of $MgH_2$ and $Mg_2NiH_4$ is investigated by thermodynamic calculations to further understand the enhanced electrochemical performance of $Nd_4Mg_{80}Ni_8H_x$. The calculated


https://doi.org/10.1021/acsnano.2c01038
ACS Nano 2022, 16, 8040−8050

formation energy of the reaction between Li and $Mg_2NiH_4$ is −1.96 eV (Figure 4c), much lower than that for the reaction between Li and $MgH_2$ (i.e., −1.04 eV) (Figure 4d), which indicates the thermodynamically favored lithiation process of $Mg_2NiH_4$ in comparison to that of $MgH_2$. Hence, during the lithiation process of the $Nd_4Mg_{80}Ni_8H_x$ electrode, $Mg_2NiH_4$ will be first reduced with the formation of $Mg_2Ni$ alloys as the discharged products, which would increase the electronic conductivity of the whole electrode and facilitate the subsequent discharge process of $MgH_2$. Conversely, $Mg_2Ni$ alloys would be oxidized to form $Mg_2NiH_4$ after the charge process of Mg, and hence, it could also act as the electronic conductor to facilitate the reversible charge process of Mg.

In addition to the role of $Mg_2NiH_4$ and $Nd_2H_5$ in enhancing the electronic conductivity of the $MgH_2$ electrode, the energy barrier of Li diffusion on the surface of $Nd_2H_5$ (111) and $Mg_2NiH_4$ (001) is calculated to be as low as 0.29 eV (Figure 4e) and 0.34 eV (Figure 4f), respectively. Both of them are much lower than the energy barrier for the Li diffusion on the surface of $MgH_2$ (110) (Figure 4g), demonstrating that the homogeneous distribution of $Mg_2NiH_4$ and $Nd_2H_5$ also plays a key role in improving the Li-ion diffusion kinetics of the $MgH_2$ electrode induced by in situ hydrogenation of single-phase $Nd_4Mg_{80}Ni_8$ alloys. Interestingly, the energy barrier of Li diffusion on the surface of Mg (0001) and $Mg_2Ni$ (010) that are formed after the lithiation process is calculated to be as low as 0.03 and 0.24 eV, respectively (Figure S7), and the energy barrier of Li diffusion on the surface of LiH (001) as verified by our previous publication is determined to be as low as 0.04 eV.[30] These results directly demonstrate that, in comparison with a high Li diffusion barrier, as observed in the delithiation process, the reversible lithiation process of Mg and $Mg_2Ni$ is kinetically favored. Electrochemical impedance spectroscopy (EIS) is further conducted to experimentally understand the Li-ion conductivity of the $Nd_4Mg_{80}Ni_8H_x$ electrode. The semicircle in the medium- and high-frequency region is attributed to the charge transfer resistance between the cathode ($Nd_4Mg_{80}Ni_8H_x$)/anode (Li) and the solid electrolyte ($LiBH_4$), and the slope line in the low-frequency region is a typical Warburg behavior, corresponding to the Li-ion diffusion kinetics of the electrode. As shown in Figure 5a, the initial semicircle of the $Nd_4Mg_{80}Ni_8H_x$ electrode is obviously smaller than that of the $MgH_2$ electrode, indicating a low electron transfer resistance at the electrode/electrolyte interface of the former electrode. In addition, the slope of the line at the frequency region for the $Nd_4Mg_{80}Ni_8H_x$ electrode is larger than that of the $MgH_2$ electrode, indicating a higher lithium-ion diffusion rate of $Nd_4Mg_{80}Ni_8H_x$ electrode. The Li ion diffusion coefficient ($D_{Li}$) of the $Nd_4Mg_{80}Ni_8H_x$ electrode (Figure 5b) at its open potential state is calculated to be $1.83 \times 10^{-9}$ $cm^2$ $s^{-1}$, almost 5 orders of magnitude higher than that of the $MgH_2$ electrode ($2.48 \times 10^{-14}$ $cm^2$ $s^{-1}$), which directly demonstrates the significant enhancement of Li-ion diffusion kinetics due to the uniform distribution of $Mg_2NiH_4$ and $Nd_2H_5$ with a Li-ion diffusion barrier lower than that of $MgH_2$, corresponding well with the theoretical calculation results. Interestingly, the uniform distribution of $Mg_2NiH_4$ and $MgH_2$ is well-maintained after repeated Li storage performance of the $Nd_4Mg_{80}Ni_8H_x$ electrode, which could be attributed to the positive role of the inactive $Nd_2H_5$ for Li storage upon cycling in preserving the structural stability of the whole electrode (Figure 3b−f). It could effectively stabilize the effect of $Nd_2H_5$ and $Mg_2NiH_5$ in promoting the electron and Li-ion conductivity of the whole electrode and hence effectively improve the reversibility of the $MgH_2$ electrode with high specific capacity. In addition, it is noticed that, in addition to the superior electron and Li-ion conductivity of $Mg_2NiH_4$ compared to those of $MgH_2$ (Figure 4a,c,d,f,g), which could kinetically facilitate the Li storage performance of $Mg_2NiH_4$, the average length of Mg−H bonds in $Mg_2NiH_4$ reaches 2.02 Å (Figure S8a,b), which is much larger than that of $MgH_2$ (i.e., 1.71 Å). It indicates the much weaker Mg−H bonds of $Mg_2NiH_4$ compared those of $MgH_2$ due to the thermodynamic destabilization effect,[31,32] which could further thermodynamically promote the reversible Li storage performance of $Mg_2NiH_4$. Induced by this thermodynamic and kinetic enhancement, a high reversible capacity of 652 mAh $g^{-1}$ could be achieved for $Mg_2NiH_4$ at 0.5C (1C = 960 mA $g^{-1}$) after 75 cycles with a capacity retention as high as 92% (Figure S9a). Moreover, even at a high current density of 1C, $Mg_2NiH_4$ is still capable of delivering a high reversible capacity of 602 mAh $g^{-1}$ after 100 cycles with a capacity retention of 85% (Figure S9a), indicating the excellent cycling stability of $Mg_2NiH_4$, which could be further supported by homogeneous distribution of $Mg_2NiH_4$ after 50 cycles at 1C (Figure S9b,c). Therefore, the relatively stable structure of $Mg_2NiH_4$ could also contribute to suppressing the phase separation of $MgH_2$ during the cycling charge and discharge process. By comparison, clear aggregation of Mg could be observed for the pure $MgH_2$ electrode after the initial discharge process in the elemental mapping results (Figure 3g,h), which indirectly confirms the obvious phase separation between Mg and LiH, leading to the rapid capacity degradation of the $MgH_2$ electrode (Figure 3i).

In addition, it is interesting to note that the $MgH_2$ electrode with the introduction of both $Mg_2NiH_4$ and $Nd_2H_5$ delivers a discharge capacity of 621 and 430 mAh $g^{-1}$ at 1 and 1.5C, respectively, which is 51 and 75% higher than that of the $MgH_2$ electrode with the introduction of $Mg_2NiH_4$ only (Figure S5b). This result provides further evidence for the effective role of $Nd_2H_5$ with high electron and Li-ion conductivity in enhancing the Li storage performance of $MgH_2$, especially at high current densities. However, the difference between the $MgH_2$ electrode modified by both $Mg_2NiH_4$ and $Nd_2H_5$ and the $MgH_2$ electrode modified by $Mg_2NiH_4$ only is actually small at a low current density of 0.5C. Therefore, in addition to considering the role of the electron and Li-ion conductivity of $Nd_2H_5$, the catalytic effect of $Mg_2NiH_4$ and $Nd_2H_5$ in enhancing the electrochemical property of $MgH_2$ is evaluated. Theoretical calculations based on density functional theory (DFT) demonstrate that two Mg−H bonds of the pristine $MgH_2$ monomer have an equal length of 1.71 Å. By comparison, the average length of Mg−H bonds in the $MgH_2$ on the surface of $Nd_2H_5$ and $Mg_2NiH_4$ is increased to 1.86 and 1.94 Å, respectively (Figure S8c,d). This result indicates that both $Nd_2H_5$ and $Mg_2NiH_4$ are capable of weakening Mg−H bonds of $MgH_2$, and $Mg_2NiH_4$ is more effective in weakening Mg−H bonds. This result could be further supported by their corresponding $H_2$ desorption tests (Figure S8e), which demonstrate that the $H_2$ desorption temperature of $MgH_2$ is significantly reduced under the catalysis of both $Mg_2NiH_4$ and $Nd_2H_5$. Particularly, the onset temperature for the $H_2$ desorption from $MgH_2$ reaches approximately 360 °C. In strong contrast, the onset temperature for the $H_2$ desorption of $MgH_2$ under the catalysis of $Mg_2NiH_4$ and $Nd_2H_5$ is significantly reduced to 196 and 290


https://doi.org/10.1021/acsnano.2c01038
ACS Nano 2022, 16, 8040−8050

°C, respectively, which is 164 and 70 °C lower than that of pure $MgH_2$. These results directly demonstrate the catalytic role of $Mg_2NiH_4$ and $Nd_2H_5$ in effectively weakening of Mg−H bonds, which hence could promote reversible Li storage performance of $MgH_2$. Considering the comparable mechanism of $H_2$ desorption and absorption of $MgH_2$ with its lithiation and delithiation process,[12,24] the catalytic role of either $Mg_2NiH_4$ or $Nd_2H_5$ could kinetically promote the lithiation and delithiation performance of $MgH_2$, resulting in an excellent electrochemical performance.

To our best knowledge, since Li ions and electrons are transported entirely in the solid phase of the ASSLIBs, the interfacial contact between solid-state electrolyte and electrodes is one of the primary factors that affects the electrochemical performance of all-solid-state batteries.[33−36] Therefore, the cross-sectional SEM images of $Nd_4Mg_{80}Ni_8H_x$|$LiBH_4$ and $MgH_2$|$LiBH_4$ at their initial state and after cycling are detected, which illustrates that the interfacial contact between the $MgH_2$ electrode and the solid electrolyte at the initial state (Figure 5f) is comparable to that of $Nd_4Mg_{80}Ni_8H_x$ electrode (Figure 5c). The continuous appearance of pores and cracks, however, could be clearly observed at the interfacial area between $MgH_2$ and $LiBH_4$ and inside the cathode upon the proceeding of the cycling process (Figure 5g,h), which could be attributed to the large volume change of $MgH_2$ and thus-induced phase separation during repeated lithiation and delithiation processes, leading to poor interfacial contact that hinders the electronic and Li-ion conductivity (Figure 3i). As a result, the charge transfer resistance ($R_{ct}$) and the SEI resistance ($R_{SEI}$) in the $MgH_2$ anode is significantly increased to 24.66 and 26.18 Ω, respectively, after only one cycle of the charge and discharge process according to the EIS profiles, which contributes to the significant capacity degradation of the $MgH_2$ electrode. By comparison, taking advantage of the role of the inactive $Nd_2H_5$ with uniform distribution on a molecular level in preserving the structural stability of the whole electrode (Figure 3i), both the structure of the $Nd_4Mg_{80}Ni_8H_x$ electrode and the interfacial contact between the $Nd_4Mg_{80}Ni_8H_x$ electrode and the solid electrolyte are well-preserved after 20 cycles at 1C (Figure 5e,d). Moreover, the surface of the $Nd_4Mg_{80}Ni_8$ electrode is still smooth without any obvious cracks after cycling (Figure S10a,b), whereas clear holes and cracks could be observed on the surface of the $MgH_2$ electrode (Figure S10c,d). This result indirectly demonstrates that the homogeneous distribution of $Nd_2H_5$ frameworks could serve as a robust host to restrain the volume change effectively of $MgH_2$ and $Mg_2NiH_4$ during the cycling, which leads to a significantly improved cycling performance. As a result, both $R_{ct}$ and $R_{SEI}$ are well-preserved and are even lowered to some extent due to the structural activation process during the first cycle of the charge and discharge process, which provides additional evidence for the stable interfacial stability of the $Nd_4Mg_{80}Ni_8H_x$ electrode. In addition, owing to the well-preserved structural integrity induced by the uniform space-confinement role of $Nd_2H_5$ frameworks with high Li-ion and electron conductivity, the Li-ion diffusion coefficient of the $Nd_4Mg_{80}Ni_8H_x$ electrode remains approximately 5 orders of magnitude higher than that of the $MgH_2$ electrode upon cycling, leading to excellent cycling stability.

## CONCLUSION

In conclusion, we report the fabrication of space-confined $MgH_2$ and $Mg_2NiH_4$ by the uniformly distributed $Nd_2H_5$ frameworks with high Li-ion and electron conductivity through the facile hydrogenation of single-phase $Nd_4Mg_{80}Ni_8$ alloys. The in situ formation of $MgH_2$ and $Mg_2NiH_4$ nanocrystals could not only shorten Li-ion and electron diffusion pathways of the whole electrode but also relieve the thus-induced stress from the large volume change of metal hydrides. The homogeneous distribution of inactive $Nd_2H_5$ frameworks based on a molecular level, on the other hand, could act as a structural host that could effectively alleviate the large volume expansion and suppress the phase separation of thus-confined $MgH_2$ and $Mg_2NiH_4$. More importantly, the uniform distribution of $Nd_2H_5$, which is theoretically and experimentally demonstrated to be an electronic conductor with a Li-ion diffusion barrier that is much lower than that of $MgH_2$ and $Mg_2NiH_4$, is capable of effectively facilitating the electron and Li-ion transfer of $MgH_2$ and $Mg_2NiH_4$. Moreover, both $Nd_2H_5$ and $Mg_2NiH_4$ are capable of catalytically weakening Mg−H bonds of $MgH_2$, which hence kinetically promote the reversible lithiation and delithiation reaction of $MgH_2$. As a result, the space-confined $MgH_2$ and $Mg_2NiH_4$ into inactive $Nd_2H_5$ frameworks deliver a reversible capacity of 997 mAh $g^{-1}$ after 100 cycles at a high current density of 2038 mA $g^{-1}$. This work provides a promising strategy to improve the Li storage performance of various metal hydrides by building Li-ion and electron conductive frameworks, and it stimulates the interest in realizing high-performance metal-hydride-based ASSLIBs for practical applications.

## MATERIALS AND METHODS

**Synthesis of $Nd_4Mg_{80}Ni_8H_x$.** The single-phase $Nd_4Mg_{80}Ni_8$ alloys were synthesized using a medium-frequency induction furnace with blocks of Nd (Sigma, ≥99.99 wt %), Mg (Sigma, ≥99.99 wt %), and Ni (Sigma, ≥99.99 wt %) as starting materials. After being ground three times, the $Nd_4Mg_{80}Ni_8$ powder was annealed at 400 °C for 2 days, followed by quenching in ice−water. The as-synthesized $Nd_4Mg_{80}Ni_8$ alloys were heated to 350 °C for 2 h under 47 bar of $H_2$ toward the activation and hydrogenation.

**Synthesis of $Nd_2H_5$ Powder.** $Nd_2H_5$ was fabricated via the hydrogenation of commercial Nd powders (500 mg, Sigma, ≥99.99 wt %). Typically, Nd powders were heated to 300 °C for 2 h under a hydrogen pressure of 60 bar to obtain $Nd_2H_5$ powders.

**Synthesis of $Mg_2NiH_4$ Powder.** In a typical process, the commercial Mg and Ni powders with a molar ratio of 2:1 were mixed by ball milling at 300 rpm for 3 h under an Ar atmosphere. Subsequently, the thus-milled composite was heated to 400 °C for 2 h under a hydrogen pressure of 70 bar to obtain $Mg_2NiH_4$ powders.

**Cell Assembly.** The schematic illustration of the preparation of the electrode and the operating cell is shown in Figure S13. The working electrode was prepared by ball milling of the metal hydrides, $LiBH_4$ (Acros, ≥95%), and conductive carbon (Super P) with a mass ratio of 1:1:2 using a planetary ball mill (QM-3SP4, Nanjing) at 400 rpm for 12 h. First, 72 mg of $LiBH_4$ powder was pressed at 400 MPa, followed by the addition of 4 mg of the electrode material, to obtain a cathode/electrolyte bilayer pellet. A Li foil disk of 9 mm diameter was added on the bottom of the solid electrolyte to serve as the anode. All of the cells were fabricated using homemade test cells, in which the battery components were placed into a polyetheretherketone (PEEK) cylinder and pressed between two stainless steel pistons serving as electrical contacts, and all sample handling and cell assembly were performed in a glovebox (Mikrouna, Shanghai) under an Ar atmosphere ($H_2O$ and $O_2$ <1 ppm).

**Material Characterization.** The phase structure of all of the samples was investigated by X-ray diffraction (D8 Advance, Bruker AXS Corporation) with Cu K$\alpha$ radiation ($\lambda$ = 1.5418 Å). The morphology of samples was observed by field emission scanning electron microscopy (JEOL 7500FA, Tokyo, Japan) and transmission


https://doi.org/10.1021/acsnano.2c01038
ACS Nano 2022, 16, 8040−8050

electron microscopy (JEOL 2011F) coupled with energy-dispersive spectrometry.

**Electrochemical Measurements.** All electrochemical tests were measured at 130 °C. The ASSLIBs with $Nd_4Mg_{80}Ni_8H_x$ as the electrode material were galvanostatically charged and discharged in a potential range from 0.3 to 1.0 V vs $Li^+/Li$ at 0.1C (1C = 2038 mA $g^{-1}$) using Neware battery test systems (CT-3008W-5 V20A-S4, Shenzhen, China). The lower-limit cyclic potential of 0.3 V was selected to avoid the irreversible formation of Li−Mg alloys below 0.3 V, which would result in significant capacity degradation during cycling.[8,37] The specific capacities of the electrode were measured based on the mass of $Nd_4Mg_{80}Ni_8H_x$. Cyclic voltammetry curves were measured at a scan rate of 0.025 mV $s^{-1}$ in the potential range of 0.3−1.0 V (vs $Li^+/Li$), and electrochemical impedance spectroscopy curves were measured in a frequency range from 100 kHz to 100 mHz. In the chronoamperometry (CA) measurement, 100 mg of electrode composite powder was added into the PEEK cylinder, followed by pressing with a pressure of 400 MPa. Thereafter, stainless steel sheets were used on both sides of the pellet as electrodes. The measurement was conducted with a constant voltage of 10 mV. The resistance and the conductivity were obtained by the following equations:

$$R = \frac{V}{I} \tag{3}$$

$$\sigma = \frac{d}{AR} \tag{4}$$

where $I$ is the current obtained by CA, $d$ is the thickness, and $A$ is the area of the electrolyte pellet. CV and CA measurements were performed using a CHI-660E electrochemistry workstation. Galvanostatic intermittent titration technique (GITT) measurements were carried out with a negative current pulse at 0.1C for 1800 s, followed by relaxation for 1800 s. This sequence of discharge pulse followed by a relaxation time was repeated until the potential reached 0.3 V.

**Computational Methods.** Density functional theory calculations were carried out using projector-augmented wave (PAW) method as implemented in Vienna ab initio simulation package (VASP).[38−40] A generalized gradient approximation (GGA) of the Perdew−Burke−Ernzerhof (PBE) functional was employed to describe the exchange-correlation interaction.[41] The DFT-D3 method was also adopted to evaluate the van der Waals interactions.[42] In all calculations, the energy cutoff was set as 500 eV, and Γ-centered $k$-point mesh with mesh point spacing less than 0.05 $Å^{-1}$ was applied. The structures were relaxed until the forces and total energy on all atoms were converged to less than 0.05 eV $Å^{-1}$ and $1 \times 10^{-5}$ eV. To obtain the energy curves of the lithiation processes, the formation energy ($E_f$) was calculated as follows:

$$E_f = \sum E_{product} - \sum E_{reactant} \tag{5}$$

where $E_{product}$ and $E_{reactant}$ are the total energy of every product and reactant in the lithiation reaction formula, respectively. A reaction with lower $E_f$ is more likely to occur thermodynamically. The diffusion of Li on the surface of $MgH_2$, $Mg_2NiH_4$, and $Nd_2H_5$ is simulated using the climbing-image nudged elastic band (CI-NEB) method.[43,44]

**Hydrogen Storage Measurements.** Temperature-programmed desorption (TPD), isothermal dehydrogenation tests, and the corresponding hydrogenation process of the as-prepared samples were conducted on a home-built high-pressure gas sorption apparatus, which was carefully calibrated by adopting $LaNi_5$ as a reference sample in terms of hydrogen storage capacity and guaranteed an accuracy of ±1%. Approximately 20 mg of as-prepared sample was used for each test. Temperature-programmed desorption tests were performed at a heating rate of 5 °C $min^{-1}$. Both TPD and isothermal dehydrogenation processes were conducted under an initial pressure of <0.001 MPa.

## ASSOCIATED CONTENT

### Supporting Information

The Supporting Information is available free of charge at https://pubs.acs.org/doi/10.1021/acsnano.2c01038.

Additional SEM, XRD, and electrochemical data; comparison of electrochemical performance; hydrogen desorption performance of metal hydrides (PDF)

## AUTHOR INFORMATION


### Corresponding Authors

**Xuebin Yu** − *Department of Materials Science, Fudan University, Shanghai 200433, China;* orcid.org/0000-0002-4035-0991; Email: yuxuebin@fudan.edu.cn

**Guanglin Xia** − *Department of Materials Science, Fudan University, Shanghai 200433, China;* orcid.org/0000-0002-3493-4309; Email: xiaguanglin@fudan.edu.cn

### Authors

**Panyu Gao** − *Department of Materials Science, Fudan University, Shanghai 200433, China*

**Shunlong Ju** − *Department of Materials Science, Fudan University, Shanghai 200433, China*

**Zipeng Liu** − *State Key Laboratory of Advanced Special Steels & Shanghai Key Laboratory of Advanced Ferrometallurgy & School of Materials Science and Engineering, Shanghai University, Shanghai 200444, China*

**Dalin Sun** − *Department of Materials Science, Fudan University, Shanghai 200433, China*

Complete contact information is available at: https://pubs.acs.org/10.1021/acsnano.2c01038


### Notes

The authors declare no competing financial interest.

## ACKNOWLEDGMENTS

This work was partially supported by the National Key R&D Program of China (No. 2020YFA0406204), National Science Fund for Distinguished Young Scholars (51625102), the National Natural Science Foundation of China (51971065, 51901045, U2130208), the Science and Technology Commission of Shanghai Municipality (No. 21ZR1407500), the Innovation Program of Shanghai Municipal Education Commission (2019-01-07-00-07-E00028), and the Programs for Professor of Special Appointment (Eastern Scholar) at Shanghai Institutions of Higher Learning.

## REFERENCES


(1) Bruce, P. G.; Scrosati, B. J.; Tarascon, M. Nanomaterials for Rechargeable Lithium Batteries. *Angew. Chem., Int. Ed.* **2008**, *47*, 2930−2946.

(2) Yang, Y.; Okonkwo, E. G.; Huang, G. Y.; Xu, S. M.; Sun, W.; He, Y. H. On the Sustainability of Lithium Ion Battery Industry-A Review and Perspective. *Energy Stor. Mater.* **2021**, *36*, 186−212.

(3) Fang, Y. J.; Zeng, Y. X.; Jin, Q.; Lu, X. F.; Luan, D. Y.; Zhang, X. T.; Lou, X. W. Nitrogen Doped Amorphous Zn-Carbon Multichannel Fibers for Stable Lithium Metal Anodes. *Angew. Chem., Int. Ed.* **2021**, *60*, 8515−8520.

(4) Jin, H. C.; Xin, S.; Chuang, C. H.; Li, W. D.; Wang, H. Y.; Zhu, J.; Xie, H. Y.; Zhang, T. M.; Wan, Y. Y.; Qi, Z. K.; Yan, W. S.; Lu, Y. R.; Chan, T. S.; Wu, X. J.; Goodenough, J. B.; Ji, H. X.; Duan, X. F. Black Phosphorus Composites with Engineered Interfaces for High-Rate High-Capacity Lithium Storage. *Science* **2020**, *370*, 192.

(5) Oumellal, Y.; Zlotea, C.; Bastide, S.; Cachet-Vivier, C.; Leonel, E.; Sengmany, S.; Leroy, L.; Aymard, L.; Bonnet, J. P.; Latroche, M. Bottom-Up Preparation of $MgH_2$ Nanoparticles with Enhanced Cycle Life Stability During Electrochemical Conversion in Li-Ion Batteries. *Nanoscale* **2014**, *6*, 14459−14466.
(6) Zhong, S. L.; Ju, S. L.; Shao, Y. F.; Chen, W.; Zhang, T. F.; Huang, Y. Q.; Zhang, H. Y.; Xia, G. L.; Yu, X. B. Magnesium Hydride Nanoparticles Anchored on MXene Sheets as High Capacity Anode for Lithium-Ion Batteries. *J. Energy Chem.* **2021**, *62*, 431−439.
(7) Cano-Banda, F.; Gallardo-Gutierrez, A.; Luviano-Ortiz, L.; Hernandez-Guerrero, A.; Jain, A.; Ichikawa, T. High Capacity $MgH_2$ Composite Electrodes for All-Solid-State Li-Ion Battery Operating at Ambient Temperature. *Int. J. Hydrog. Energy* **2021**, *46*, 1030−1037.
(8) Oumellal, Y.; Rougier, A.; Nazri, G. A.; Tarascon, J. M.; Aymard, L. Metal Hydrides for Lithium-Ion Batteries. *Nat. Mater.* **2008**, *7*, 916−921.
(9) Cheng, Q. H.; Sun, D. L.; Yu, X. B. Metal Hydrides for Lithium-Ion Battery Application: A Review. *J. Alloys Compd.* **2018**, *769*, 167−185.
(10) Aymard, L.; Oumellal, Y.; Bonnet, J. P. Metal Hydrides: An Innovative and Challenging Conversion Reaction Anode for Lithium-Ion Batteries. *Beilstein J. Nanotechnol.* **2015**, *6*, 1821−1839.
(11) Zhang, B. P.; Si, Y. S.; Gu, Q. F.; Chen, M.; Yu, X. B. Hydrangea-Shaped 3D Hierarchical Porous Magnesium Hydride-Carbon Framework with High Rate Performance for Lithium Storage. *ACS Appl. Mater. Interfaces* **2019**, *11*, 28987−28995.
(12) Zeng, L.; Kawahito, K.; Ikeda, S.; Ichikawa, T.; Miyaoka, H.; Kojima, Y. Metal Hydride-Based Materials Towards High Performance Negative Electrodes for All-Solid-State Lithium-Ion Batteries. *Chem. Commun.* **2015**, *51*, 9773−9776.
(13) Brutti, S.; Meggiolaro, D.; Paolone, A.; Reale, P. Magnesium Hydride as Negative Electrode Active Material in Lithium Cells: A Review. *Mater. Today Energy* **2017**, *3*, 53−59.
(14) Zhang, B. P.; Xia, G. L.; Sun, D. L.; Fang, F.; Yu, X. B. Magnesium Hydride Nanoparticles Self-Assembled on Graphene as Anode Material for High-Performance Lithium-Ion Batteries. *ACS Nano* **2018**, *12*, 3816−3824.
(15) Chen, S. M.; Wen, K. H.; Fan, J. T.; Bando, Y. S.; Golberg, D. Progress and Future Prospects of High-Voltage and High-Safety Electrolytes in Advanced Lithium Batteries: From Liquid to Solid Electrolytes. *J. Mater. Chem. A* **2018**, *6*, 11631−11663.
(16) Fan, L.; Wei, S. Y.; Li, S. Y.; Li, Q.; Lu, Y. Y. Recent Progress of the Solid-State Electrolytes for High-Energy Metal-Based Batteries. *Adv. Energy Mater.* **2018**, *8*, 1702657.
(17) Famprikis, T.; Canepa, P.; Dawson, J. A.; Islam, M. S.; Masquelier, C. Fundamentals of Inorganic Solid-State Electrolytes for Batteries. *Nat. Mater.* **2019**, *18*, 1278−1291.
(18) Duchêne, L.; Remhof, A.; Hagemann, H.; Battaglia, C. Status and Prospects of Hydroborate Electrolytes for All-Solid-State Batteries. *Energy Stor. Mater.* **2020**, *25*, 782−794.
(19) Yang, X. F.; Adair, K. R.; Gao, X. J.; Sun, X. L. Recent Advances and Perspectives on Thin Electrolytes for High-Energy-Density Solid-State Lithium Batteries. *Energy Environ. Sci.* **2021**, *14*, 643−671.
(20) Matsuo, M.; Orimo, S. Lithium Fast-Ionic Conduction in Complex Hydrides: Review and Prospects. *Adv. Energy Mater.* **2011**, *1*, 161−172.
(21) Zettl, R.; Gombotz, M.; Clarkson, D.; Greenbaum, S. G.; Ngene, P.; de Jongh, P. E.; Wilkening, H. M. R. Li-Ion Diffusion in Nanoconfined $LiBH_4$-LiI/$Al_2O_3$: From 2D Bulk Transport to 3D Long-Range Interfacial Dynamics. *ACS Appl. Mater. Interfaces* **2020**, *12*, 38570−38583.
(22) Liu, H.; Ren, Z. H.; Zhang, X.; Hu, J. J.; Gao, M. X.; Pan, H. G.; Liu, Y. F. Incorporation of Ammonia Borane Groups in the Lithium Borohydride Structure Enables Ultrafast Lithium Ion Conductivity at Room Temperature for Solid-State Batteries. *Chem. Mater.* **2020**, *32*, 671−678.
(23) Zhang, T. F.; Wang, Y. M.; Song, T.; Miyaoka, H.; Shinzato, K.; Miyaoka, H.; Ichikawa, T.; Shi, S. Q.; Zhang, X. G.; Isobe, S.; et al. Ammonia, A switch for Controlling High Ionic Conductivity in Lithium Borohydride Ammoniates. *Joule* **2018**, *2*, 1522−1533.
(24) Dao, A. H.; Berti, N.; López-Aranguren, P.; Zhang, J. X.; Cuevas, F.; Jordy, C.; Latroche, M. Electrochemical Properties of $MgH_2$-$TiH_2$ Nanocomposite as Active Materials for All-Solid-State Lithium Batteries. *J. Power Sources* **2018**, *397*, 143−149.
(25) Huang, L.; Aymard, L.; Bonnet, J. P. $MgH_2$-$TiH_2$ Mixture As an Anode for Lithium-Ion Batteries: Synergic Enhancement of the Conversion Electrode Electrochemical Performance. *J. Mater. Chem. A* **2015**, *3*, 15091−15096.
(26) El Kharbachi, A.; Uesato, H.; Kawai, H.; Wenner, S.; Miyaoka, H.; Sørby, M. H.; Fjellvag, H.; Ichikawa, T.; Hauback, B.ør. C. $MgH_2$-CoO: A Conversion-Type Composite Electrode for $LiBH_4$-Based All-Solid-State Lithium Ion Batteries. *RSC Adv.* **2018**, *8*, 23468−23474.
(27) Xia, G. L.; Zhang, B. P.; Chen, X. W.; Sun, D. L.; Guo, Z. P.; Liang, F. X.; Zou, W. D.; Yang, Z. Z.; Yu, X. B. Molecular-Scale Functionality on Graphene to Unlock the Energy Capabilities of Metal Hydrides for High-Capacity Lithium-Ion Batteries. *ACS Nano* **2018**, *12*, 8177−8186.
(28) Ikeda, S.; Ichikawa, T.; Kawahito, K.; Hirabayashi, K.; Miyaoka, H.; Kojima, Y. Anode Properties of Magnesium Hydride Catalyzed with Niobium Oxide for an All Solid-State Lithium-Ion Battery. *Chem. Commun.* **2013**, *49*, 7174−7176.
(29) Cuevas, F.; Korablov, D.; Latroche, M. Synthesis, Structural and Hydrogenation Properties of Mg-Rich $MgH_2$-$TiH_2$ Nanocomposites Prepared By Reactive Ball Milling Under Hydrogen Gas. *Phys. Chem. Chem. Phys.* **2012**, *14*, 1200−1211.
(30) Zhang, H. Y.; Ju, S. L.; Xia, G. L.; Sun, D. L.; Yu, X. B. Dendrite-Free Li-Metal Anode Enabled by Dendritic Structure. *Adv. Funct. Mater.* **2021**, *31*, 2009712.
(31) Kim, D.; Zhang, K.; Cho, M.; Kang, Y. M. Critical Design Factors for Kinetically Favorable P-Based Compounds Toward Alloying With Na Ions for High-Power Sodium-Ion Batteries. *Energy Environ. Sci.* **2019**, *12*, 1326−1333.
(32) Song, K. M.; Liu, C. T.; Mi, L. W.; Chou, S. L.; Chen, W. H.; Shen, C. Y. Recent Progress on the Alloy-Based Anode for Sodium-Ion Batteries and Potassium-Ion Batteries. *Small* **2021**, *17*, 1903194.
(33) Tan, D. H. S.; Banerjee, A.; Chen, Z.; Meng, Y. S. From Nanoscale Interface Characterization to Sustainable Energy Storage Using All-Solid-State Batteries. *Nat. Nanotechnol.* **2020**, *15*, 170−180.
(34) Zhao, C. Z.; Zhao, B. C.; Yan, C.; Zhang, X. Q.; Huang, J. Q.; Mo, Y. F.; Xu, X. X.; Li, H.; Zhang, Q. Liquid Phase Therapy to Solid Electrolyte-Electrode Interface in Solid-State Li Metal Batteries: A Review. *Energy Stor. Mater.* **2020**, *24*, 75−84.
(35) Wang, S.; Sun, Q. F.; Peng, W. X.; Ma, Y.; Zhou, Y.; Song, D. W.; Zhang, H. Z.; Shi, X. X.; Li, C. L.; Zhang, L. Q. Ameliorating the Interfacial Issues of All-Solid-State Lithium Metal Batteries by Constructing Polymer/Inorganic Composite Electrolyte. *J. Energy Chem.* **2021**, *58*, 85−93.
(36) Chen, X. Z.; He, W. J.; Ding, L. X.; Wang, S. Q.; Wang, H. H. Enhancing Interfacial Contact in All Solid State Batteries with a Cathode-Supported Solid Electrolyte Membrane Framework. *Energy Environ. Sci.* **2019**, *12*, 938−944.
(37) Brutti, S.; Mulas, G.; Piciollo, E.; Panero, S.; Reale, P. Magnesium Hydride as a High Capacity Negative Electrode for Lithium Ion Batteries. *J. Mater. Chem.* **2012**, *22*, 14531−14537.
(38) Kresse, G.; Hafner, J. Ab initio Molecular Dynamics for Liquid Metals. *Phys. Rev. B* **1993**, *47*, 558−561.
(39) Kresse, G.; Furthmüller, J. Efficient Iterative Schemes for ab initio Total-Energy Calculations Using a Plane-Wave Basis Set. *Phys. Rev. B* **1996**, *54*, 11169−11186.
(40) Blochl, P.; Blöchl, E.; Blöchl, P. Projected Augmented-Wave Method. *Phys. Rev. B* **1994**, *50*, 17953−17979.
(41) Perdew, J. P.; Burke, K.; Ernzerhof, M. Generalized Gradient Approximation Made Simple. *Phys. Rev. Lett.* **1996**, *77*, 3865−3868.
(42) Grimme, S.; Antony, J.; Ehrlich, S.; Krieg, H. A Consistent and Accurate ab initio Parametrization of Density Functional Dispersion Correction (DFT-D) for the 94 Elements H-Pu. *J. Chem. Phys.* **2010**, *132*, 154104.


https://doi.org/10.1021/acsnano.2c01038
ACS Nano 2022, 16, 8040−8050

(43) Paier, J.; Hirschl, R.; Marsman, M.; Kresse, G. The Perdew-Burke-Ernzerhof Exchange-Correlation Functional Applied to the G2−1 Test Set Using a Plane-Wave Basis Set. *J. Chem. Phys.* **2005**, *122*, 234102.
(44) Heyden, A.; Bell, A. T.; Keil, F. J. Efficient methods for finding transition states in chemical reactions: Comparison of Improved Dimer Method and Partitioned Rational Function Optimization Method. *J. Chem. Phys.* **2005**, *123*, 224101.

## Recommended by ACS

**Experimental Investigation and First-Principles Calculations of a $Ni_3Se_4$ Cathode Material for Mg-Ion Batteries**

Luyao Wei, Yingjin Wei, *et al.*
FEBRUARY 07, 2020
ACS APPLIED MATERIALS & INTERFACES
READ

**$MoS_2$/CN/$Fe_{0.95}S_{1.05}$ with a Hierarchical Architecture as a Long-Durable Anode for Sodium Ion Batteries**

Hongyi Chen, Qiming Liu, *et al.*
OCTOBER 21, 2021
ACS APPLIED ENERGY MATERIALS
READ

**Influence Mechanism of $Mg^{2+}$ Doping on Electrochemical Properties of $LiFePO_4$ Cathode Materials**

Xingzhong Liu, Fuliang Zhu, *et al.*
JUNE 16, 2022
ACS APPLIED ENERGY MATERIALS
READ

**Engineering the Proton-Substituted $HNaV_6O_{16}\cdot 4H_2O$ Cathode for the Ultrafast-Charging Zinc Storage**

Leyuan Shi, Linlin Zhang, *et al.*
FEBRUARY 10, 2022
ACS SUSTAINABLE CHEMISTRY & ENGINEERING
READ

**Get More Suggestions >**



https://doi.org/10.1021/acsnano.2c01038
*ACS Nano* 2022, 16, 8040−8050